

# General Oriented Synthesis of Precise Carbon-Confined Nanostructures by Low-Pressure Vapor Superassembly and Controlled Pyrolysis

Jiashen Meng,<sup>†</sup> Xiong Liu,<sup>†</sup> Jiantao Li,<sup>†</sup> Qi Li,<sup>†</sup> Chuan Zhao,<sup>‡</sup> Linhan Xu,<sup>§</sup> Xuanpeng Wang,<sup>†</sup> Fang Liu,<sup>†</sup> Wei Yang,<sup>†</sup> Xiaoming Xu,<sup>†</sup> Ziang Liu,<sup>†</sup> Chaojiang Niu,<sup>\*,†,||</sup> and Liqiang Mai<sup>\*,†,||</sup>

<sup>†</sup>State Key Laboratory of Advanced Technology for Materials Synthesis and Processing, International School of Materials Science and Engineering, Wuhan University of Technology, Wuhan 430070, China

<sup>‡</sup>School of Chemistry, Faculty of Science, The University of New South Wales, Sydney, New South Wales 2052, Australia

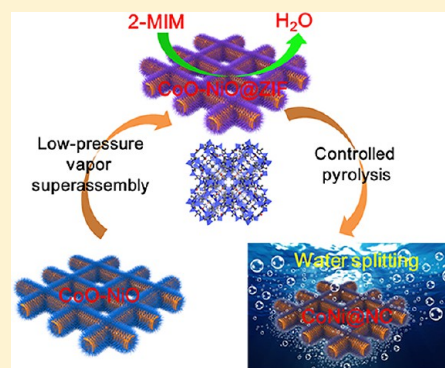
<sup>§</sup>Department of Physics and Collaborative Innovation Center for Optoelectronic Semiconductors and Efficient Devices, Xiamen University, Xiamen 361005, China

<sup>||</sup>Department of Chemistry, University of California, Berkeley, California 94720, United States

## Supporting Information

**ABSTRACT:** Earth-abundant metal-based nanostructured materials have been widely studied for potential energy conversion and storage. However, controlled synthesis of functional nanostructures with high electron conductivity, high reaction activity, and structural stability is still a formidable challenge for further practical applications. Herein, for the first time, we develop a facile, efficient, and general method for the oriented synthesis of precise carbon-confined nanostructures by low-pressure vapor superassembly of a thin metal–organic framework (MOF) shell and subsequent controlled pyrolysis. The selected nanostructured metal oxide precursors not only act as metal ion sources but also orient the superassembly of gaseous organic ligands through the coordination reactions under the low-pressure condition, resulting in the formation of a tunable MOF shell on their surfaces. This strategy is further successfully extended to obtain various precise carbon-confined nanostructures with diverse compositions and delicate morphologies. Notably, these as-prepared carbon-confined architectures exhibit outstanding electrochemical performances in water splitting and lithium storage. The remarkable performances are mainly attributed to the synergistic effect from appropriate chemical compositions and stable carbon-confined structures. This synthetic approach and proposed mechanism open new avenues for the development of functional nanostructured materials in many frontier fields.

**KEYWORDS:** General synthesis, carbon-confined nanostructures, MOF shell, vapor superassembly, energy conversion and storage



Developing energy conversion and storage devices with high efficiency, low cost, and environmental benignity is of great significance in addressing the problems of increasingly worsening environmental pollution and the impending exhaustion of fossils.<sup>1,2</sup> More efficient energy conversion and storage devices have been developed to meet these future energy requirements, including water splitting, fuel cell, metal–air batteries, lithium-ion batteries (LIBs), etc.<sup>3–6</sup> The energy conversion efficiency of electrochemical water splitting is dependent on both anodic oxygen evolution reaction (OER) and cathodic hydrogen evolution reaction (HER).<sup>7</sup> To improve the energy conversion efficiency of water splitting, it is highly desired to develop efficient electrocatalysts to minimize the decomposition/polarization voltage between OER and HER. To date, precious ruthenium-/iridium-based and platinum-based nanocomposites are regarded as remarkable OER and HER electrocatalysts, respectively.<sup>8</sup> However, the high cost and low abundance greatly limit their further practical applications.

Intensive efforts have been focused on developing safe LIBs with high energy/power density, high cycling stability, and low cost. However, due to the relatively low theoretical capacity (372 mAh·g<sup>-1</sup>) of commercial graphite, the current commercial LIBs have reached their performance limits. Therefore, developing low-cost and earth-abundant metal-based nanostructured materials with outstanding electrochemical performances on energy conversion and storage devices is of great significance for both fundamental studies and practical applications.

Intensive efforts have been dedicated to developing efficient strategies for synthesizing earth-abundant metal-based functional materials.<sup>7,9–12</sup> As ideal electrodes, the functional

**Received:** September 15, 2017

**Revised:** October 26, 2017

**Published:** November 13, 2017

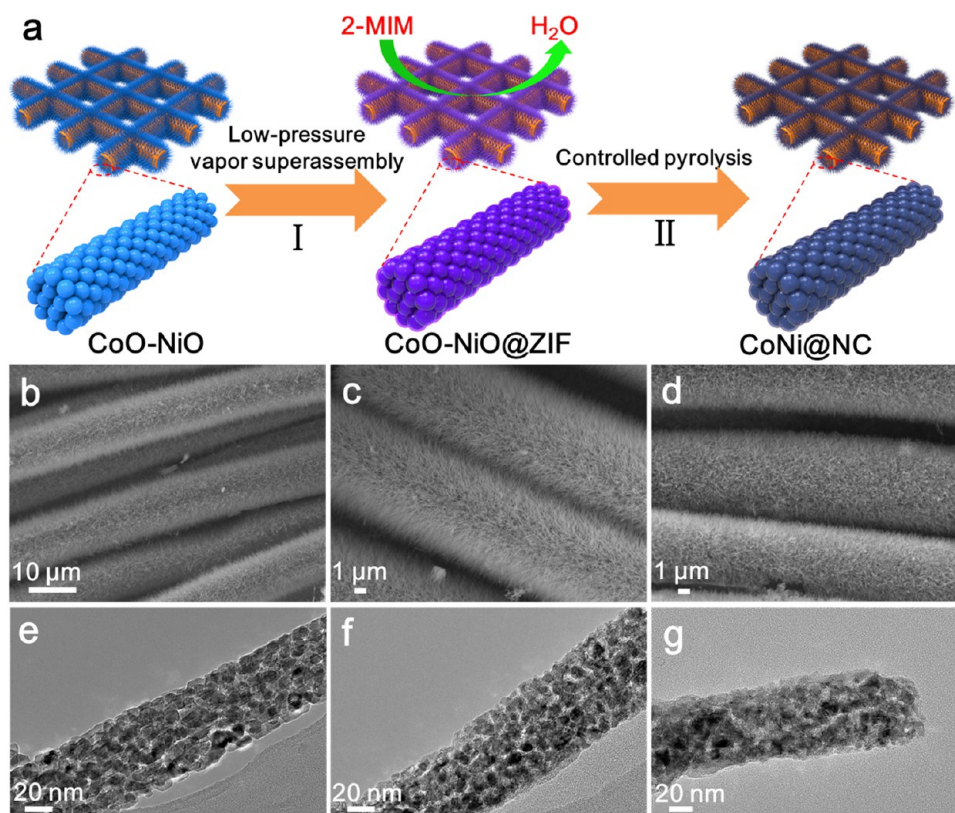


**Figure 1.** Synthesis and characterization of N-doped carbon-confined CoNi (CoNi@NC) mesoporous nanowire arrays on carbon cloth. (a) Schematics of the formation process of CoNi@NC mesoporous nanowire arrays on carbon cloth. First, the gaseous organic ligands react with CoO–NiO at 120 °C under low-pressure condition, forming ZIF-confined CoO–NiO (CoO–NiO@ZIF) nanowire arrays on carbon cloth; the confined MOFs subsequently convert into N-doped carbon at 500 °C under Ar/H<sub>2</sub> (95:5 vol %) condition, finally obtaining CoNi@NC mesoporous nanowire arrays on carbon cloth. (b–g) Corresponding SEM and TEM images of CoO–NiO (b,e), CoO–NiO@ZIF (c,f), and CoNi@NC (d,g) nanowire arrays on carbon cloth, respectively.

materials should fulfill these requirements, such as high specific surface area, excellent reaction activity, good stability, high electronic conductivity, and low cost. Generally, one typical way is to design and synthesize multilevel structures with interior spaces and abundant interfaces.<sup>13–20</sup> These architectures can provide a high specific surface area, short transport path, large active sites, and good strain accommodation, thereby resulting in enhanced electrochemical performances. Another efficient method is to construct carbon-based composites to improve the structural stability and electronic conductivity.<sup>21–24</sup> For instance, Liang et al. reported Co<sub>3</sub>O<sub>4</sub> nanocrystals on graphene as a synergistic catalyst with higher oxygen reduction reaction activity than that of simplex Co<sub>3</sub>O<sub>4</sub> nanoparticles.<sup>25</sup> To combine both merits, it remains a formidable challenge to develop a facile and general strategy for obtaining uniform carbon-confined multilevel nanostructures with desirable compositions and delicate morphologies. In previous reports, atomic layer deposition technique is a versatile controllable method to deposit nanoscale films of metal oxides on substrate surfaces.<sup>26</sup> However, the high cost, low yield, and limited coating compositions of this technology seriously hinder its practical applications.

Metal–organic frameworks (MOFs), a typical porous crystalline material, are assembled and created by the coordination bonds between metal ions/clusters and organic ligands.<sup>27</sup> Their unique properties of high surface area, tunable porosity, and controlled structures endow MOFs with great potential applications in the past few decades.<sup>28,29</sup> Recently,

MOF-derived materials have attracted great interests in energy conversion and storage.<sup>30–33</sup> For example, Pachfule et al. reported one-dimensional carbon nanorods with excellent supercapacitor performance derived from rod-shaped MOFs.<sup>34</sup> Despite great advancements, these derived architectures are highly limited and dependent on the morphologies and components of MOFs. In addition, to realize well-confined carbon onto various as-prepared nanostructures, researchers have focused on preferentially forming uniform MOF nanocoating. Zhang et al. synthesized ZnO@MOFs core–shell nanorod arrays on carbon cloth by an ion exchange method.<sup>35</sup> Very recently, Cai et al. reported a versatile strategy for the controllable synthesis of three-dimensional MOF hybrid arrays by utilizing semiconducting nanostructures as self-sacrificing templates in the reaction solution.<sup>36</sup> However, it still remains a great challenge to accurately confine the growth of MOFs on the core surfaces rather than in precursor solutions, especially for multilevel nanostructures.

Considering the advantages of MOF superstructures, in this work, we develop a facile, efficient, and general method for the oriented synthesis of precise carbon-confined nanostructures by low-pressure vapor superassembly and subsequent controlled pyrolysis. This strategy is based on the *in situ* oriented formation of MOFs on the surfaces of as-prepared metal oxide nanostructures due to the coordination reactions with gaseous organic ligands under the low-pressure condition. This versatile method can be generally applied to fabricate many carbon-confined nanostructures with various compositions and delicate

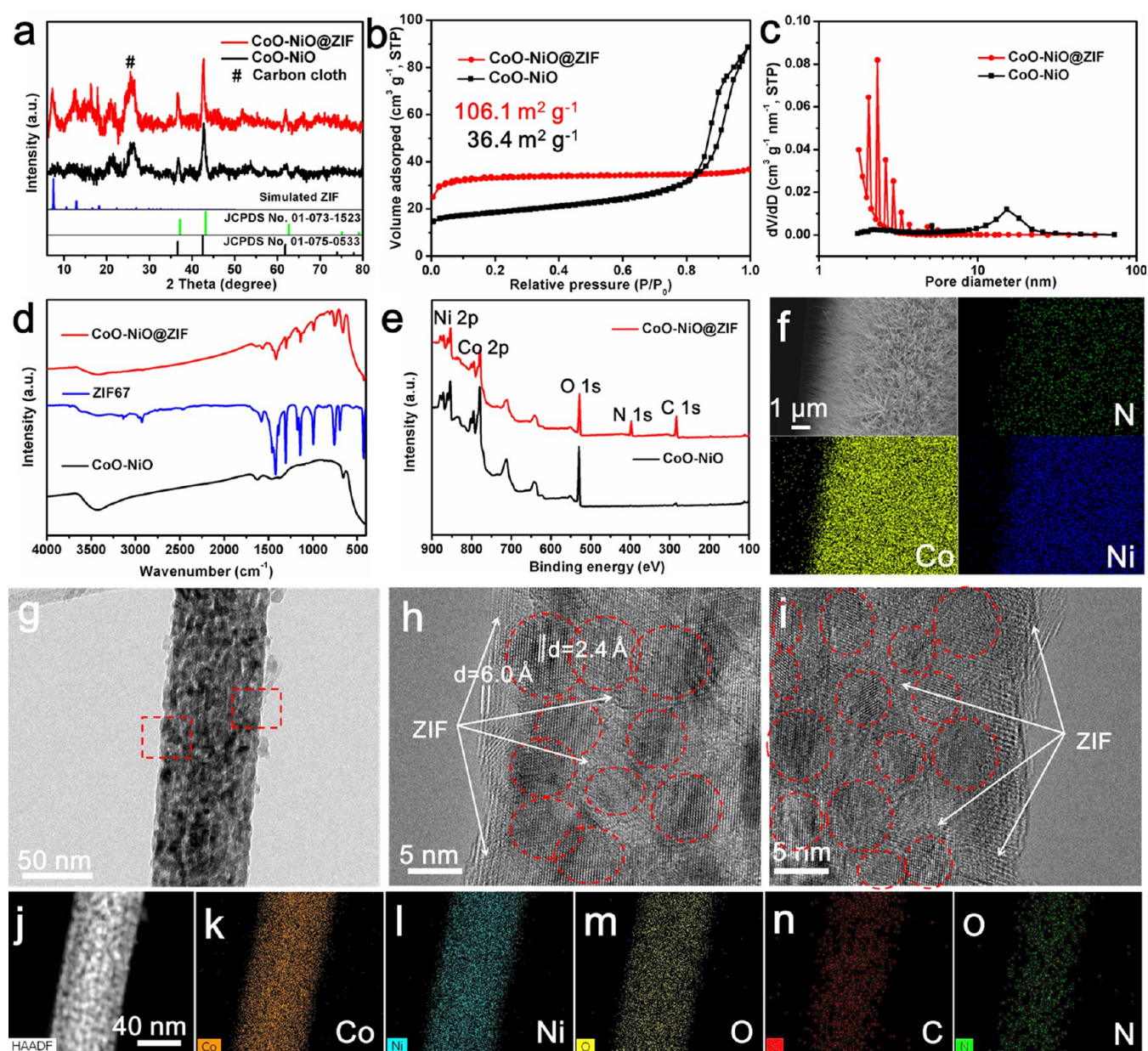


**Figure 2.** Characterizations of the formation of ZIF shell on CoO–NiO nanowire arrays. (a) XRD patterns of CoO–NiO and CoO–NiO@ZIF nanowire arrays. (b,c)  $N_2$  adsorption–desorption isotherms and pore size distribution of CoO–NiO and CoO–NiO@ZIF nanowire arrays. (d) FTIR spectra of CoO–NiO nanowire arrays, CoO–NiO@ZIF nanowire arrays, and ZIF-67 crystals. (e) XPS spectra of CoO–NiO and CoO–NiO@ZIF nanowire arrays. (f) Elemental mapping images of CoO–NiO@ZIF nanowire arrays for N, Co, and Ni. (g–i) TEM and HRTEM images of single CoO–NiO@ZIF nanowire (red circles are residual CoO–NiO nanocrystals). (j–o) HAADF-STEM image and the corresponding EDX mappings of single CoO–NiO@ZIF nanowire for Co, Ni, O, C, and N images.

morphologies. The carbon layers with tunable thickness and controlled dopants endow these architectures with high activity, evitable aggregation, easy electronic conduction, and good structural protection. Consequently, these as-synthesized carbon-confined nanostructures exhibit excellent electrochemical performance on water splitting and lithium storage.

**Results and Discussion. Mechanism of Oriented Synthesis.** The overall synthetic procedure for N-doped carbon-confined CoNi (CoNi@NC) mesoporous nanowire arrays on carbon cloth is presented in Figure 1a. The CoO–NiO mesoporous nanowire arrays on carbon cloth were first synthesized (Figure S1). These mesoporous nanowires exhibit uniform morphology ( $\sim 60$  nm in diameter and  $\sim 2$   $\mu\text{m}$  in

length) and consist of small nanoparticles (approximately 5–15 nm in diameter) (Figure 1b,e). Then, the as-prepared CoO–NiO mesoporous nanowire arrays on carbon cloth and solid organic ligands (2-methylimidazole, 2-MIM) were both treated at 120  $^\circ\text{C}$  under a low pressure ( $\sim 100$  Pa) condition in one system. The solid 2-MIM powders convert into gases and fill the whole reaction system. These gaseous organic ligands react with as-prepared CoO–NiO mesoporous nanowire arrays on carbon cloth, forming in situ zeolitic imidazolate framework (ZIF) shells on them (CoO–NiO@ZIF) (Figure 1c). These nanostructured metal oxides oriented the superassembly of gaseous organic ligands to form ZIF. The surface of mesoporous nanowire shows obvious thin ZIF shell (Figure

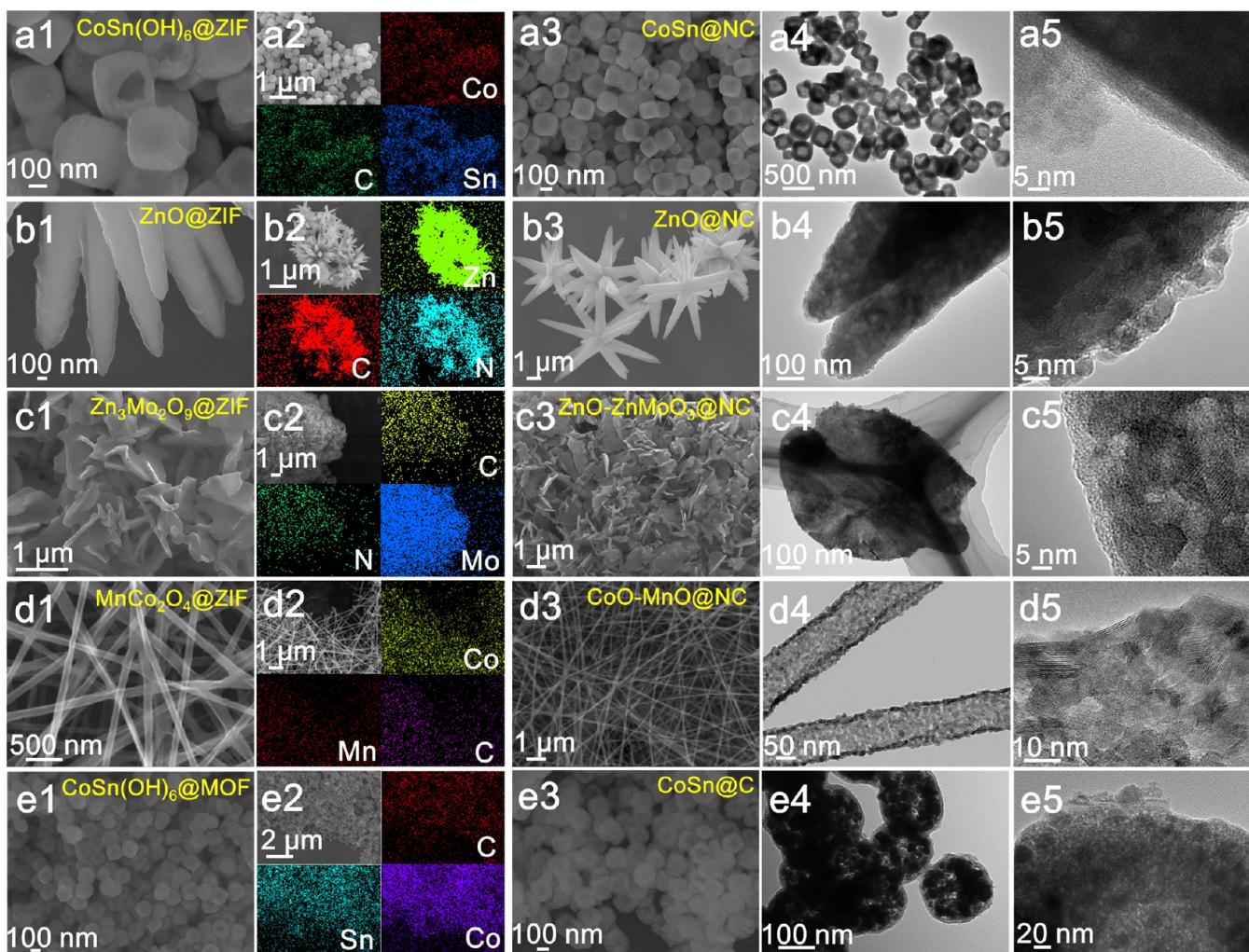
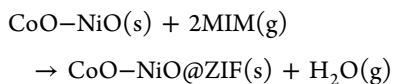


**Figure 3.** Generality and versatility of the oriented synthesis strategy. (a1,a2) SEM image and elemental mapping images of  $\text{CoSn(OH)}_6@ZIF$  hollow nanocubes. (a3–a5) SEM and TEM images of derived  $\text{CoSn@NC}$  nanocubes. (b1,b2) SEM image and elemental mapping images of  $\text{ZnO@ZIF}$  nanorods. (b3–b5) SEM and TEM images of derived  $\text{ZnO@NC}$  nanorods. (c1,c2) SEM image and elemental mapping images of  $\text{Zn}_3\text{Mo}_2\text{O}_9@ZIF$  nanosheets. (c3–c5) SEM and TEM images of derived  $\text{ZnO-ZnMoO}_3@NC$  nanosheets. (d1,d2) SEM image and elemental mapping images of  $\text{MnCo}_2\text{O}_4@ZIF$  mesoporous nanotubes. (d3–d5) SEM and TEM images of derived  $\text{CoO-MnO@NC}$  mesoporous nanotubes. (e1,e2) SEM image and elemental mapping images of  $\text{CoSn(OH)}_6@MOF$  hollow nanocubes. (e3–e5) SEM and TEM images of derived  $\text{CoSn@C}$  hollow nanocubes.

1f), and the surfaces of nanoparticles in mesoporous nanowires become rough, indicating that gaseous organic ligands diffuse into the interior mesopores in nanowires and react with the nanoparticles. The proposed reaction equation based on this low-pressure vapor superassembly method is shown as follows:



During this process, due to the deprotonation of organic ligands, the generated gaseous water volatilizes away from the reaction interfaces. Because of uniform distribution of gaseous organic ligands in the whole system, this interfacial reaction results in the formation of uniform ZIF shell, and the shell thickness can be easily tuned by controlling reaction temperature and time. As shown in Figure S2, by contrast, the appropriate reaction condition is 120 °C and 8 h. However, when treated at higher temperature and/or longer time, the complete conversion occurs from metal oxide templates to large ZIF crystals (Figure S3). Eventually, after controlled pyrolysis under  $\text{Ar/H}_2$  (95:5 vol %) condition, the morphol-

ogy-preserved carbon-confined  $\text{CoNi}$  mesoporous nanowire arrays on carbon cloth are obtained, which are composed of uniform mesoporous nanowires with small nanoparticles inside thin carbon shells (Figure 1d,g). In brief, this strategy comprises the oriented growth of MOFs by low-pressure vapor superassembly on nanostructured metal oxides and *in situ* formation of carbon coatings via the following controlled pyrolysis, which can be applied to obtain various nanostructures with delicate morphologies and rich compositions.

To further prove the formation of ZIF shell on the  $\text{CoO-NiO}$  nanowire arrays, a series of characterizations were carried out after low-pressure vapor superassembly treatment (Figure 2). X-ray diffraction (XRD) patterns show clear diffraction peaks from the simulated ZIF ( $\text{Co-ZIF-67}$ ),  $\text{CoO}$ , and  $\text{NiO}$  phases, indicating the existence of ZIF (Figure 2a). The nitrogen adsorption–desorption isotherm of  $\text{CoO-NiO@ZIF}$  nanowire powder shows a high Brunauer–Emmett–Teller (BET) specific surface area of  $106.1 \text{ m}^2\cdot\text{g}^{-1}$ , which is about three times that of pure  $\text{CoO-NiO}$  ( $36.4 \text{ m}^2\cdot\text{g}^{-1}$ ) (Figure 2b). The typical Langmuir isotherms vary from type IV to type I, indicating the formation of microporous structure. The

corresponding pore size distribution is from approximately 10–15 nm to below 4 nm (Figure 2c). The decreased pore size indicates that the mesopores in CoO–NiO nanowires are filled with the formed ZIF nanocrystals. On the basis of Fourier-transform infrared (FTIR) spectra, the typical vibrations of ZIF crystals also appear in those of CoO–NiO@ZIF nanowire arrays (Figure 2d). In addition, X-ray photoelectron spectroscopy (XPS) and elemental mapping analyses confirm the presence and distribution of Co, Ni, and N (Figure 2e,f). Further high-resolution transmission electron microscopy (HRTEM) analyses clearly indicate that mesoporous nanowires and the nanoparticles in them are uniformly coated by ZIF layers, which demonstrates that nanostructured metal oxides orient the superassembly of gaseous organic ligands (Figure 2g–i). A large interlayer spacing of  $\sim 6.0$  Å can be observed, belonging to ZIF nanocrystals. The interior nanoparticles display a relatively small interlayer spacing of  $\sim 2.4$  Å, which corresponds to the (111) lattice plane of CoO–NiO. A high-angle annular dark-field scanning transmission electron microscopy (HAADF-STEM) image further confirmed the single nanowire is composed of uniform nanoparticles, and the corresponding energy-dispersive X-ray (EDX) mappings show that the Co, Ni, O, N, and C elements are distributed homogeneously over all single nanowires (Figure 2j–o). Therefore, all the results demonstrate that the formation of ZIF shell occurs on the CoO–NiO nanowire arrays by low-pressure vapor superassembly. In addition, a more uniform coating layer can be achieved more easily whether on the surface of a bulk or in the nanopores compared with the solution reaction coating.

**Generality and Versatility of the Oriented Synthesis Strategy.** To confirm the generality and versatility of our strategy, various morphology-preserved carbon-confined nanostructures are also obtained according to the aforementioned procedures (Figure 3). First, various metal oxide nanostructures with different morphologies and compositions were synthesized, including CoSn(OH)<sub>6</sub> hollow nanocubes, ZnO nanorods, Zn<sub>3</sub>Mo<sub>2</sub>O<sub>9</sub> nanosheets, and MnCo<sub>2</sub>O<sub>4</sub> mesoporous nanotubes (Figures S4–S8). The detailed synthesis procedures are clearly illustrated in the experimental section, [Supporting Information](#). Scanning electron microscopy (SEM) and TEM images show that these obtained structures possess uniform and delicate morphologies. The corresponding XRD patterns show high crystallinity and pure phases. Subsequently, when the as-synthesized metal oxide nanostructures and organic ligand powders were treated under the low-pressure condition, the gaseous organic ligands react with nanostructured metal oxides, forming the MOF shell by coordination reactions. More importantly, to testify the versatility of this strategy, we also adopt other organic ligands, such as 1,4-dicarboxybenzene (H<sub>2</sub>BDC) (Figure 3e1–e5). For example, the similar reaction equation is shown as follows: CoSn(OH)<sub>6</sub>(s) + H<sub>2</sub>BDC(g) → CoSn(OH)<sub>6</sub>@MOF(s) + H<sub>2</sub>O(g). SEM images, TEM images, elemental mapping images, and XRD patterns give more direct evidence for the formation of MOFs coating. Because the gaseous organic ligands can uniformly diffuse onto the surfaces of various metal oxide nanostructures, these reaction processes on them are well controlled. Finally, after controlled pyrolysis, the carbon-confined nanostructures are obtained, including CoSn@NC nanocubes, ZnO@NC nanorods, ZnO–ZnMoO<sub>3</sub>@NC nanosheets, CoO–MnO@NC mesoporous nanotubes, and CoSn@C hollow nanocubes (Figure 3). These architectures exhibit uniform morphology-preserved

structures and thin carbon coatings on them. Overall, this strategy can be widely applied to obtain carbon-confined architectures with dedicate morphologies.

In our strategy, the key to the formation of precise confined carbon is obtaining the uniform and stable MOF shells. The generated MOFs on metal oxides act as the precursors for carbon sources. By adjusting organic ligands, the heteroatoms (e.g., N, etc.) can be easily introduced into the carbon frameworks, which may lead to more novel properties. First, the selected metal oxides have great influence on the formation of MOFs. The selected metal oxides, acting as the sources of inorganic ions/clusters, should be able to easily react with gaseous organic ligands and form the corresponding MOFs. The binding energies between metal ions and oxygen ions also influence the formation rates of MOFs. This reaction process undergoes the bond breaking in metal oxides and the formation of new coordination bonds between metal ions/clusters and gaseous organic ligands. On the basis of density functional theoretical (DFT) calculations, the bonding energies of various metal oxides were shown in Table S1. When the selected metal oxides have small bonding energies (e.g., ZnO, CoO, NiO, and SnO), their bonds can be easily broken, tending to react first with gaseous organic ligands. Interestingly, although SnO has lower bonding energy of  $\sim 249.6$  kJ·mol<sup>-1</sup> than those of ZnO and CoO (261.8 and 279.8 kJ·mol<sup>-1</sup>), it still remains difficult to form MOF shell (Figure S9). It is because the mismatched coordination reaction between Sn<sup>2+</sup> and 2-MIM cannot form long-range order structure. Inversely, some metal oxides with strong covalent bonds cannot react with gaseous organic ligands. Taking MgO nanoparticles as an example, the corresponding XRD patterns and elemental mapping images demonstrated no formation of MOFs on their surfaces (Figure S10). Apart from common metal oxides, the selected metal oxides can be also extended to metal hydroxides, metal carbonates, etc. Therefore, the selected metal oxides should fulfill both small bonding energy and well-defined coordination reaction. In addition, the easy sublimation of solid organic ligands into gases is another key point for the formation of MOFs. The selected organic ligands, usually including small molecules, possess relatively low boiling point and strong coordination ability. Finally, the low pressure is crucial in obtaining stable and precise MOF shells, which can be controlled by modulating the vacuum oven. During the synthesis process, the low pressure can efficiently decrease the boiling points and increase the concentrations of organic ligands in the reaction system, thereby stimulating the formation of MOFs. However, the low pressure is beneficial for the removal of generated water from the surfaces of nanostructures, avoiding the dissolution of MOFs and so allowing the formation of stable MOF shells.

In brief, for the precise formation of MOFs on the as-prepared metal oxide nanostructures, there are three main requirements: (1) selected metal oxides, (2) easy sublimation of organic ligands, and (3) low-pressure condition. Therefore, compared with current main coating strategies, this oriented method is a facile, efficient, and general strategy for controlling the formation of MOFs on various as-prepared metal oxide nanostructures, thereby realizing precise carbon layers confined onto them (Table S2).

**Electrocatalytic Performance.** The CoO–NiO@ZIF nanowire arrays on carbon cloth were treated at different temperatures (500, 600, and 700 °C), resulting in CoNi@NC-500, CoNi@NC-600, and CoNi@NC-700 samples (mass

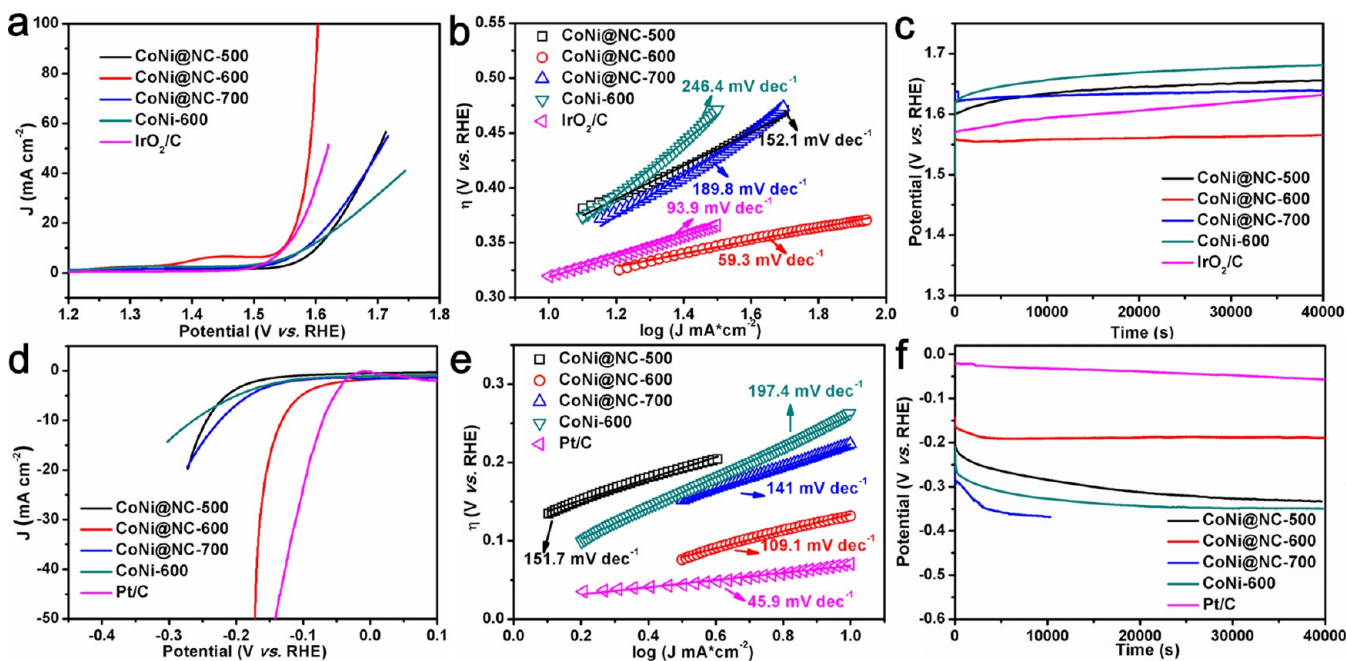


**Figure 4.** Electrocatalytic performances of various catalysts for OER and HER in 1.0 M KOH. (a) *iR*-compensated OER polarization curves of CoNi@NC-500, CoNi@NC-600, CoNi@NC-700, CoNi-600, and IrO<sub>2</sub>/C samples at a scan rate of 5 mV·s<sup>-1</sup>. (b,c) Corresponding Tafel plots and chronopotentiometric tests under a constant current density of 10 mA·cm<sup>-2</sup>. (d) *iR*-compensated HER polarization curves of CoNi@NC-500, CoNi@NC-600, CoNi@NC-700, CoNi-600, and Pt/C samples at a scan rate of 5 mV·s<sup>-1</sup>. (e,f) Corresponding Tafel plots and chronopotentiometric tests under a constant current density of -10 mA·cm<sup>-2</sup>.

loading:  $\sim 2.0$  mg·cm<sup>-2</sup>). These samples still exhibit similar integrated morphologies (Figure S11). The corresponding XRD patterns show pure CoNi alloying phases (Figures S12 and S13). The CoNi nanowire arrays on carbon cloth (CoNi-600) were also obtained for a comparison (Figure S14). The *iR* correction was applied to all initial data to minimize the effect of ohmic resistance (Figure S15f). The linear sweep voltammetry (LSV) curves were carried out to compare the OER activity of all catalysts (Figure 4a). There is no doubt that the commercial IrO<sub>2</sub>/C shows excellent OER activity with relatively low overpotential, whereas bare CoNi-600 without the surface modification has poor OER activity. With ultrathin carbon coating, the OER catalytic activity of CoNi@NC is improved due to the synergistic effect between coating carbon and CoNi alloy. It is clearly observed that the CoNi@NC-600 electrode shows a much higher current density at an earlier onset potential compared with CoNi-600. The CoNi@NC-600 electrode needs the overpotentials of 317, 338, 361, and 374 mV to afford 10, 20, 50, and 100 mA·cm<sup>-2</sup>, respectively. To reach 10 mA·cm<sup>-2</sup>, the overpotentials of CoNi@NC-500, CoNi@NC-700, CoNi-600, and IrO<sub>2</sub>/C are 371, 353, 366, and 320 mV, respectively. The catalytic kinetics for oxygen evolution were evaluated (Figure 4b). The Tafel slope of CoNi@NC-600 (59.3 mV·dec<sup>-1</sup>) is much lower than that of CoNi-600 (246.4 mV·dec<sup>-1</sup>), implying improved OER kinetics after surface coating. This value is also lower than those of IrO<sub>2</sub>/C (93.9 mV·dec<sup>-1</sup>), CoNi@NC-500 (152.1 mV·dec<sup>-1</sup>), and CoNi@NC-700 (189.8 mV·dec<sup>-1</sup>). Electrochemically active surface areas (ECSAs) were estimated from the double-layer capacitance (C<sub>dl</sub>) by cyclic voltammetry (CV) measurements in the non-Faradaic region. The C<sub>dl</sub> value of CoNi@NC-600 is 301.3 mF cm<sup>-2</sup>, much higher than those of CoNi@NC-500, CoNi@NC-700, and CoNi-600 samples (Figure S15). Furthermore, the long-term stabilities of all

catalysts were probed using chronopotentiometric tests (Figure 4c). After continual 40000 s of testing, both IrO<sub>2</sub>/C and CoNi-600 catalysts have great potential degradation of 61.6 and 71.0 mV with a constant current of 10 mA·cm<sup>-2</sup>, respectively. CoNi@NC-500 and CoNi@NC-700 possess relatively good durability with degradation of 53.9 and 17.9 mV, respectively. By contrast, the as-prepared CoNi@NC-600 possesses the lowest potential and the best durability with just small degradation of 6.5 mV. Overall, the CoNi@NC-600 sample exhibits excellent OER performance, which can be comparable to other popular OER catalysts in previous works (Figure S17a).<sup>17,37–43</sup>

The HER performances of different CoNi@NC, CoNi-600, and Pt/C samples were also assessed in 1.0 M KOH (Figure 4d–f). From polarization curves in Figure 4d, as expected, the commercial Pt/C shows excellent HER activity, and the overpotential is 71 mV at -10 mA·cm<sup>-2</sup>. CoNi-600 catalyst has poor HER activity, and the overpotential is 264 mV at -10 mA·cm<sup>-2</sup>. After carbon coating, the HER activities of CoNi-based catalysts have been improved. The overpotentials of CoNi@NC-500, CoNi@NC-600, and CoNi@NC-700 samples are 244, 132, and 224 mV at -10 mA·cm<sup>-2</sup>, respectively. The CoNi@NC-600 sample possesses efficient hydrogen evolution closed to the catalytic activity of Pt/C and is comparable to those already reported materials (Figure S17b).<sup>39,43–49</sup> From Tafel plots in Figure 4e, even though the Tafel slope of commercial Pt/C is 45.9 mV·dec<sup>-1</sup>, the CoNi@NC-600 sample possesses a relatively low Tafel slope of 109.1 mV·dec<sup>-1</sup>, indicating a Volmer–Heyrovsky mechanism, and obviously lower than those of CoNi-600 (197.4 mV·dec<sup>-1</sup>), CoNi@NC-500 (151.7 mV·dec<sup>-1</sup>), and CoNi@NC-700 (141.0 mV·dec<sup>-1</sup>) samples. On the basis of CV analyses in the non-Faradaic region, the C<sub>dl</sub> value of CoNi@NC-600 is also much higher than those of other samples (Figure S16). The long-term

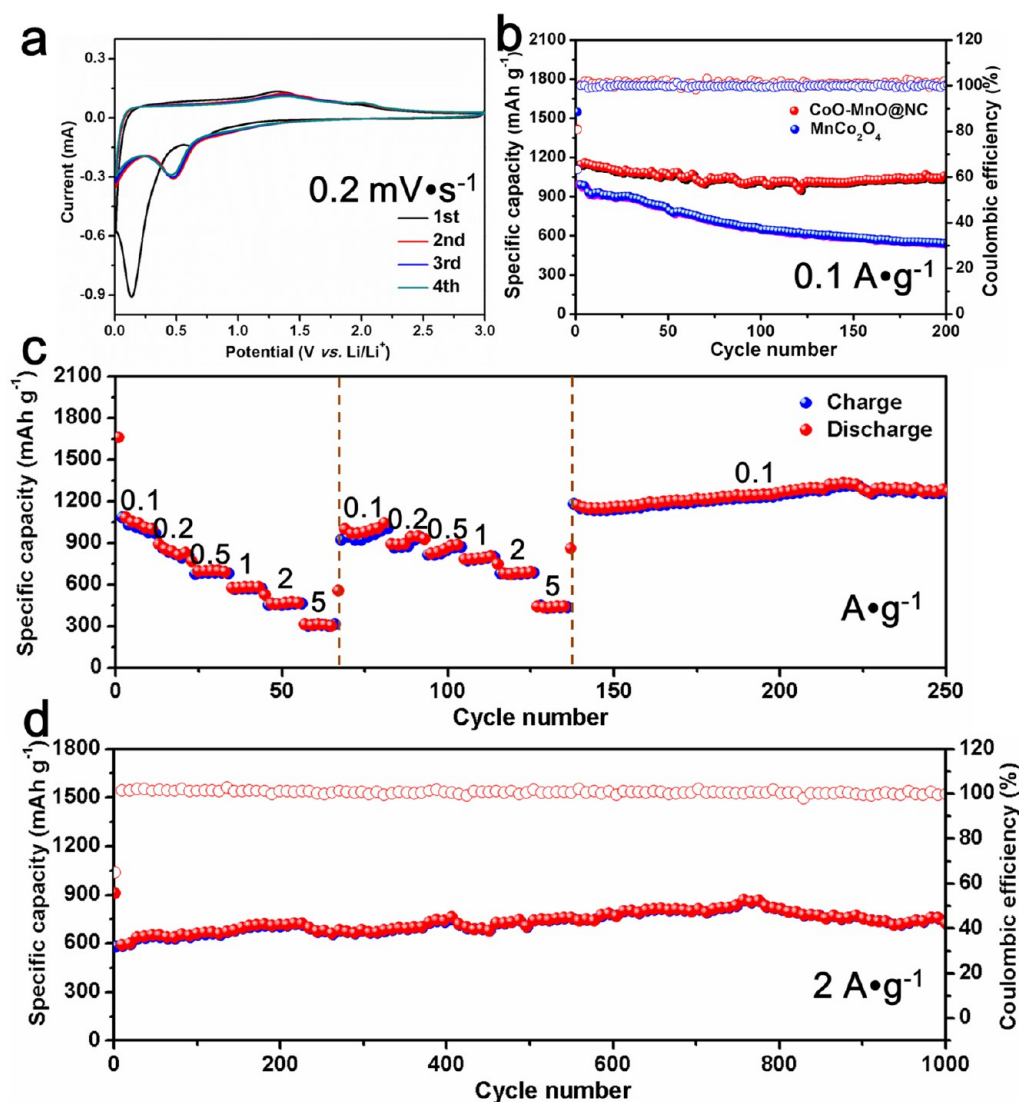


**Figure 5.** Lithium storage performances of CoO–MnO@NC and MnCo<sub>2</sub>O<sub>4</sub> mesoporous nanotubes. (a) First four CV curves tested at a scan rate of 0.2 mV·s<sup>-1</sup> in the potential range from 0.01 to 3.0 V versus Li<sup>+</sup>/Li. (b) Cycling performance and Coulombic efficiency tested at a current density of 0.1 A·g<sup>-1</sup>. (c) Rate performance tested at current densities of 0.1, 0.2, 0.5, 1, 2, and 5 A·g<sup>-1</sup>. (d) Cycling performance and Coulombic efficiency tested at a high current density of 2 A·g<sup>-1</sup>.

stabilities of all catalysts were also measured by using chronopotentiometric tests (Figure 4f). The CoNi@NC-600 sample possesses good stability with just a small degradation of 29.5 mV at a constant current density of  $-10 \text{ mA}\cdot\text{cm}^{-2}$  after 40 000 s of testing, which is lower than that of Pt/C (36.0 mV). CoNi-600, CoNi@NC-500, and CoNi@NC-700 have poor stability and obviously increased potentials.

In brief, the confined nitrogen-doped carbon layers endow the CoNi@NC-600 sample with high activity, high conductivity, and good structure stability for excellent OER and HER performances. The enhanced electronic conductivity of CoNi@NC-600 catalyst was also measured using a standard four-probe method on pressed pellets (Figure S18). Furthermore, the OER and HER catalytic mechanisms are insightfully discussed. During OER process, the CoNi nanoalloys confined into carbon layers are surface oxidized to CoNiO<sub>x</sub> via *in situ* transformation (Figure S19). Actually, the derived CoNiO<sub>x</sub> shells are real active OER catalysts, which is in accordance with previous reports.<sup>50</sup> For HER process, the contributions from CoNi nanoalloys and nitrogen dopants

synergistically increase electron density of confined carbon shells, resulting in superior HER activity.<sup>51</sup> For practical application, we assembled and measured the catalytic performance of CoNi@NC-600 for full water splitting using a two-electrode setup (CoNi@NC-600||CoNi@NC-600) in 1.0 M KOH (Figure S20a). The long-term stability of this full water-splitting setup was also examined (Figure S20b). It shows that the initial potential of 1.678 V is needed to reach  $10 \text{ mA}\cdot\text{cm}^{-2}$  and that the potential is maintained at around 1.727 V after 70 000 s. This setup just needs a potential of 1.661 V to afford a  $10 \text{ mA}\cdot\text{cm}^{-2}$  water-splitting current (Figure S20c). After 70 000 s of testing, the potential slightly changes to 1.702 V, indicating good water-splitting stability.

**Lithium Storage Performances.** To further reveal the multifunctional applications, CoO–MnO@NC and MnCo<sub>2</sub>O<sub>4</sub> mesoporous nanotubes were also used as an anode material for LIBs (Figures 5, S21, and S22). First, the CV measurements were carried out to characterize the electrochemical reaction process in the range from 0.01 to 3.0 V versus Li<sup>+</sup>/Li at a scan rate of 0.2 mV·s<sup>-1</sup>. From the latter three cycles, two pairs of

redox peaks correspond to the reduction/oxidation of both CoO and MnO; the overlapped curves indicate high electrochemical reversibility. When tested at a current density of  $0.1 \text{ A}\cdot\text{g}^{-1}$ , the first Coulombic efficiency of CoO–MnO@NC mesoporous nanotubes is 80.7%, higher than that of  $\text{MnCo}_2\text{O}_4$  mesoporous nanotubes (64%). After 200 cycles, the CoO–MnO@NC electrode exhibits higher specific capacity and higher capacity retention ( $1153 \text{ mAh}\cdot\text{g}^{-1}$  and 91.1%), than those of  $\text{MnCo}_2\text{O}_4$  electrode ( $534 \text{ mAh}\cdot\text{g}^{-1}$  and 53.9%). In addition, when tested at various current densities of 0.1, 0.2, 0.5, 1, 2, 5 and back to  $0.1 \text{ A}\cdot\text{g}^{-1}$ , the CoO–MnO@NC electrode can recover approximately 100% of its initial capacity, indicating excellent cycling stability. Even when tested at a high current density of  $2 \text{ A}\cdot\text{g}^{-1}$ , the CoO–MnO@NC electrode remains stable after 1000 cycles. Moreover, kinetic analyses show obvious lithiation pseudocapacitive behavior, which is beneficial for high-rate performance (Figure S23).<sup>52</sup> After cycling, the morphology of CoO–MnO@NC nanotubes can be maintained, further confirming their structural stability (Figure S23g,h). Compared with nanostructured mixed metal oxides in previous works, the as-synthesized CoO–MnO@NC mesoporous nanotubes exhibit excellent cycling stability and high rate performance (Table S3). These excellent performances are mainly attributed to the delicate structural motifs of CoO–MnO@NC nanotubes, such as large specific surface area, high electron conductivity, short path length, good strain accommodation, and robust structure (Figure S24).

**Conclusions.** We develop a facile and general method to synthesize *in situ* precise carbon-confined nanostructures with various compositions and delicate morphologies by a well-designed process of low-pressure vapor superassembly and subsequent controlled pyrolysis. This formation mechanism was clearly revealed and further applied to obtain various carbon-confined nanostructures. The confined carbon layers with tunable thickness and controlled dopants endow these architectures with high activity, evitable aggregation, high electronic conduction, and good structural protection, beneficial for energy conversion and storage. As proof-of-concept applications, the CoNi@NC mesoporous nanowire arrays on carbon cloth exhibit high electrocatalytic activity, high current density, and excellent stability for OER and HER compared to CoNi catalyst. Employed as an anode material for LIBs, CoO–MnO@NC mesoporous nanotubes possess high specific capacity, high rate capability, and good cycling performance. On the basis of experimental analyses, the structure–property correlations were also further demonstrated. Therefore, our work represents a new synthetic strategy for developing carbon-based functional materials for energy conversion and storage devices.

## ■ ASSOCIATED CONTENT

### Supporting Information

The Supporting Information is available free of charge on the ACS Publications website at DOI: [10.1021/acs.nanolett.7b03982](https://doi.org/10.1021/acs.nanolett.7b03982).

Material synthesis, characterization details, XRD patterns, SEM images, TEM images, elemental mapping images, Raman spectra, BET and BJH curves, XPS spectra, electrochemical characterizations, and DFT calculation details on bonding energies (PDF)

## ■ AUTHOR INFORMATION

### Corresponding Authors

\*E-mail: [mlq518@whut.edu.cn](mailto:mlq518@whut.edu.cn).

\*E-mail: [niuchaojiang11@whut.edu.cn](mailto:niuchaojiang11@whut.edu.cn).

### ORCID

Chuan Zhao: 0000-0001-7007-5946

Liqiang Mai: 0000-0003-4259-7725

### Author Contributions

J.S.M. and X.L. contributed equally to this work. L.Q.M. and J.S.M. conceived and designed the overall experiments. J.S.M. and X.L. prepared and characterized the nanomaterials. J.S.M., J.T.L., Q.L., C.Z., and C.J.N. analyzed the results. L.H.X. performed the calculations. All authors contributed to the discussion of the results and commented on the manuscript.

### Notes

The authors declare no competing financial interest.

## ■ ACKNOWLEDGMENTS

This work was supported by the National Key Research and Development Program of China (2016YFA0202603), the National Basic Research Program of China (2013CB934103), the Programme of Introducing Talents of Discipline to Universities (B17034), the National Natural Science Foundation of China (51521001), the National Natural Science Fund for Distinguished Young Scholars (51425204), the Fundamental Research Funds for the Central Universities (WUT: 2016III001 and 2016-YB-004), and State Key Laboratory of Advanced Technology for Materials Synthesis and Processing (WUT: 2015-KF-3, 2017-KF-2). We are grateful to Bichao Xu and Pei Zhang of the Core Facility and Technical Support, Wuhan Institute of Virology for technical support in transmission electron microscopy. We thank Prof. Peidong Yang of University of California, Berkeley for strong support and stimulating discussions. L.M. gratefully acknowledges financial support from China Scholarship Council (No. 201606955096).

## ■ REFERENCES

- Chu, S.; Cui, Y.; Liu, N. *Nat. Mater.* **2017**, *16*, 16–22.
- Lu, J.; Chen, Z.; Ma, Z.; Pan, F.; Curtiss, L. A.; Amine, K. *Nat. Nanotechnol.* **2016**, *11*, 1031–1038.
- Yang, Z.; Zhang, J.; Kintner-Meyer, M. C.; Lu, X.; Choi, D.; Lemmon, J. P.; Liu, J. *Chem. Rev.* **2011**, *111*, 3577–3613.
- Mai, L.; Tian, X.; Xu, X.; Chang, L.; Xu, L. *Chem. Rev.* **2014**, *114*, 11828–11862.
- Shao, M.; Chang, Q.; Dodelet, J. P.; Chenitz, R. *Chem. Rev.* **2016**, *116*, 3594–3657.
- Wang, X.; Lu, X.; Liu, B.; Chen, D.; Tong, Y.; Shen, G. *Adv. Mater.* **2014**, *26*, 4763–4782.
- Jiao, Y.; Zheng, Y.; Jaroniec, M.; Qiao, S. Z. *Chem. Soc. Rev.* **2015**, *44*, 2060–2086.
- Li, M.; Zhao, Z.; Cheng, T.; Fortunelli, A.; Chen, C.-Y.; Yu, R.; Zhang, Q.; Gu, L.; Merinov, B. V.; Lin, Z.; Zhu, E.; Yu, T.; Jia, Q.; Guo, J.; Zhang, L.; Goddard, W. A., III; Huang, Y.; Duan, X. *Science* **2016**, *354*, 1414–1419.
- Zhao, Y.; Li, X.; Yan, B.; Xiong, D.; Li, D.; Lawes, S.; Sun, X. *Adv. Energy Mater.* **2016**, *6*, 1502175.
- Tang, Y.; Zhang, Y.; Li, W.; Ma, B.; Chen, X. *Chem. Soc. Rev.* **2015**, *44*, 5926–5940.
- Wang, J.; Zhong, H. X.; Wang, Z. L.; Meng, F. L.; Zhang, X. B. *ACS Nano* **2016**, *10*, 2342–2348.
- Peng, L.; Xiong, P.; Ma, L.; Yuan, Y.; Zhu, Y.; Chen, D.; Luo, X.; Lu, J.; Amine, K.; Yu, G. *Nat. Commun.* **2017**, *8*, 15139.
- Zhao, Y.; Jiang, L. *Adv. Mater.* **2009**, *21*, 3621–3638.

- (14) Niu, C.; Meng, J.; Wang, X.; Han, C.; Yan, M.; Zhao, K.; Xu, X.; Ren, W.; Zhao, Y.; Xu, L.; Zhang, Q.; Zhao, D.; Mai, L. *Nat. Commun.* **2015**, *6*, 7402.
- (15) Liu, Y.; Luo, Y.; Elzatahry, A. A.; Luo, W.; Che, R.; Fan, J.; Lan, K.; Al-Enizi, A. M.; Sun, Z.; Li, B.; Liu, Z.; Shen, D.; Ling, Y.; Wang, C.; Wang, J.; Gao, W.; Yao, C.; Yuan, K.; Peng, H.; Tang, Y.; Deng, Y.; Zheng, G.; Zhou, G.; Zhao, D. *ACS Cent. Sci.* **2015**, *1*, 400–408.
- (16) Zhang, L.; Wu, H. B.; Lou, X. W. *J. Am. Chem. Soc.* **2013**, *135*, 10664–10672.
- (17) Meng, J.; Niu, C.; Liu, X.; Liu, Z.; Chen, H.; Wang, X.; Li, J.; Chen, W.; Guo, X.; Mai, L. *Nano Res.* **2016**, *9*, 2445–2457.
- (18) Chao, D.; Zhu, C.; Xia, X.; Liu, J.; Zhang, X.; Wang, J.; Liang, P.; Lin, J.; Zhang, H.; Shen, Z. X.; Fan, H. *J. Nano Lett.* **2015**, *15*, 565–573.
- (19) Chen, D.; Peng, L.; Yuan, Y.; Zhu, Y.; Fang, Z.; Yan, C.; Chen, G.; Shahbazian-Yassar, R.; Lu, J.; Amine, K.; Yu, G. *Nano Lett.* **2017**, *17*, 3907–3913.
- (20) Fang, Z.; Peng, L.; Lv, H.; Zhu, Y.; Yan, C.; Wang, S.; Kalyani, P.; Wu, X.; Yu, G. *ACS Nano* **2017**, *11*, 9550–9557.
- (21) Deng, D.; Yu, L.; Chen, X.; Wang, G.; Jin, L.; Pan, X.; Deng, J.; Sun, G.; Bao, X. *Angew. Chem., Int. Ed.* **2013**, *52*, 371–375.
- (22) Wu, Z. Y.; Xu, X. X.; Hu, B. C.; Liang, H. W.; Lin, Y.; Chen, L. F.; Yu, S. H. *Angew. Chem., Int. Ed.* **2015**, *54*, 8179–8183.
- (23) Li, D.; Lv, C.; Liu, L.; Xia, Y.; She, X.; Guo, S.; Yang, D. *ACS Cent. Sci.* **2015**, *1*, 261–269.
- (24) Wang, J.; Li, K.; Zhong, H. X.; Xu, D.; Wang, Z. L.; Jiang, Z.; Wu, Z. J.; Zhang, X. B. *Angew. Chem., Int. Ed.* **2015**, *54*, 10530–10534.
- (25) Liang, Y.; Li, Y.; Wang, H.; Zhou, J.; Wang, J.; Regier, T.; Dai, H. *Nat. Mater.* **2011**, *10*, 780–786.
- (26) Wang, X.; Yushin, G. *Energy Environ. Sci.* **2015**, *8*, 1889–1904.
- (27) Howarth, A. J.; Liu, Y.; Li, P.; Li, Z.; Wang, T. C.; Hupp, J. T.; Farha, O. K. *Nat. Rev. Mater.* **2016**, *1*, 15018.
- (28) Stassen, I.; Styles, M.; Grecni, G.; Van Gorp, H.; Vanderlinden, W.; De Feyter, S.; Falcaro, P.; De Vos, D.; Vereecken, P.; Ameloot, R. *Nat. Mater.* **2016**, *15*, 304–310.
- (29) Meng, J.; Niu, C.; Xu, L.; Li, J.; Liu, X.; Wang, X.; Wu, Y.; Xu, X.; Chen, W.; Li, Q.; Zhu, Z.; Zhao, D.; Mai, L. *J. Am. Chem. Soc.* **2017**, *139*, 8212–8221.
- (30) Li, S.-L.; Xu, Q. *Energy Environ. Sci.* **2013**, *6*, 1656–1683.
- (31) Wu, R.; Wang, D. P.; Rui, X.; Liu, B.; Zhou, K.; Law, A. W.; Yan, Q.; Wei, J.; Chen, Z. *Adv. Mater.* **2015**, *27*, 3038–3044.
- (32) Xia, W.; Qu, C.; Liang, Z.; Zhao, B.; Dai, S.; Qiu, B.; Jiao, Y.; Zhang, Q.; Huang, X.; Guo, W.; Dang, D.; Zou, R.; Xia, D.; Xu, Q.; Liu, M. *Nano Lett.* **2017**, *17*, 2788–2795.
- (33) Xu, Y. T.; Xiao, X.; Ye, Z. M.; Zhao, S.; Shen, R.; He, C. T.; Zhang, J. P.; Li, Y.; Chen, X. M. *J. Am. Chem. Soc.* **2017**, *139*, 5285–5288.
- (34) Pachfule, P.; Shinde, D.; Majumder, M.; Xu, Q. *Nat. Chem.* **2016**, *8*, 718–724.
- (35) Zhang, G.; Hou, S.; Zhang, H.; Zeng, W.; Yan, F.; Li, C. C.; Duan, H. *Adv. Mater.* **2015**, *27*, 2400–2405.
- (36) Cai, G.; Zhang, W.; Jiao, L.; Yu, S.-H.; Jiang, H.-L. *Chem.* **2017**, *2*, 791–802.
- (37) Bae, S.-H.; Kim, J.-E.; Randriamahazaka, H.; Moon, S.-Y.; Park, J.-Y.; Oh, I.-K. *Adv. Energy Mater.* **2017**, *7*, 1601492.
- (38) Han, L.; Yu, X. Y.; Lou, X. W. *Adv. Mater.* **2016**, *28*, 4601–4605.
- (39) Jin, H.; Wang, J.; Su, D.; Wei, Z.; Pang, Z.; Wang, Y. *J. Am. Chem. Soc.* **2015**, *137*, 2688–2694.
- (40) Li, S.; Wang, Y.; Peng, S.; Zhang, L.; Al-Enizi, A. M.; Zhang, H.; Sun, X.; Zheng, G. *Adv. Energy Mater.* **2016**, *6*, 1501661.
- (41) Liang, H.; Meng, F.; Caban-Acevedo, M.; Li, L.; Forticaux, A.; Xiu, L.; Wang, Z.; Jin, S. *Nano Lett.* **2015**, *15*, 1421–1427.
- (42) Xia, C.; Jiang, Q.; Zhao, C.; Hedhili, M. N.; Alshareef, H. N. *Adv. Mater.* **2016**, *28*, 77–85.
- (43) Yang, F.; Zhao, P.; Hua, X.; Luo, W.; Cheng, G.; Xing, W.; Chen, S. *J. Mater. Chem. A* **2016**, *4*, 16057–16063.
- (44) Feng, Y.; Yu, X.-Y.; Paik, U. *Chem. Commun.* **2016**, *52*, 1633–1636.
- (45) Han, A.; Chen, H.; Zhang, H.; Sun, Z.; Du, P. *J. Mater. Chem. A* **2016**, *4*, 10195–10202.
- (46) Jiao, L.; Zhou, Y.-X.; Jiang, H.-L. *Chem. Sci.* **2016**, *7*, 1690–1695.
- (47) Liu, T.; Asiri, A. M.; Sun, X. *Nanoscale* **2016**, *8*, 3911–3915.
- (48) Xi, W.; Ren, Z.; Kong, L.; Wu, J.; Du, S.; Zhu, J.; Xue, Y.; Meng, H.; Fu, H. *J. Mater. Chem. A* **2016**, *4*, 7297–7304.
- (49) Zhu, W.; Yue, X.; Zhang, W.; Yu, S.; Zhang, Y.; Wang, J.; Wang, J. *Chem. Commun.* **2016**, *52*, 1486–1489.
- (50) Jin, S. *ACS Energy Lett.* **2017**, *2*, 1937–1938.
- (51) Deng, J.; Ren, P.; Deng, D.; Bao, X. *Angew. Chem., Int. Ed.* **2015**, *54*, 2100–2104.
- (52) Chao, D.; Zhu, C.; Yang, P.; Xia, X.; Liu, J.; Wang, J.; Fan, X.; Savilov, S. V.; Lin, J.; Fan, H. J.; Shen, Z. X. *Nat. Commun.* **2016**, *7*, 12122.